4D electron tomography of dislocations undergoing electron irradiation

Alexandre Mussi, Philippe Carrez, Karine Gouriet, Benoit Hue, Patrick Cordier

Comptes Rendus

Physique

Alexandre Mussi, Philippe Carrez, Karine Gouriet, Benoit Hue
and Patrick Cordier

4D electron tomography of dislocations undergoing electron irradiation

Plasticity and Solid State Physics / *Plasticité et Physique des Solides*

4D electron tomography of dislocations undergoing electron irradiation

Alexandre Mussi[*],[●] *[a]*, **Philippe Carrez**[●] *[a]*, **Karine Gouriet**[●] *[a]*, **Benoit Hue**[●] *[a]*
and Patrick Cordier[●] *[a, b]*

[a] Univ Lille, CNRS, INRAE, Centrale Lille, UMR 8207 - UMET - Unité Matériaux Et
Transformations, F-59000 Lille, France

[b] Institut Universitaire de France, 1 rue Descartes, F-75005 Paris, France

E-mails: alexandre.mussi@univ-lille.fr (A. Mussi), philippe.carrez@univ-lille.fr
(P. Carrez), karine.gouriet@univ-lille.fr (K. Gouriet), benoit.hue@univ-lille.fr (B. Hue),
patrick.cordier@univ-lille.fr (P. Cordier)

Abstract. Imaging dislocation microstructures in 3D and monitoring their interactions over time is a major
challenge. In this study, we show that enhancing the contrast of dislocation lines prior to reconstruction, al-
lows to optimize an acquisition phase with fewer images and thus to follow the 3D evolution of a microstruc-
ture over time. We illustrate this new possibility by studying the first stages of formation of helical dislocations
in MgO under electron irradiation. We highlight the role of segment mobility on the initiation of climb and
reveal the existence of preferential mixed climb planes.

Keywords. Dislocation, Electron tomography, Irradiation, Helical dislocations, MgO.

Online first, 29th June 2021

1. Introduction

The mechanical properties of materials depend to a large extent on the defects they contain
and the way they interact with each other, and over time, under the influence of various factors
(temperature, stress, irradiation, etc.). Transmission electron microscopy (TEM) has long been
the preferred tool for the study of crystal defects. However, with dislocations, often present in
large numbers and with complex geometries, the fact of having only 2D projections according to
a limited angular range represents a severe limitation. Tomography is one of the natural answers
to this question and has given rise to numerous applications both in the field of materials, even
at atomic resolution [1] and in biology [2]. Yet, the application of this technique to dislocations
is particularly delicate because of the extreme sensitivity of the contrast to the orientation with
the diffraction vector and it was only in 2006 that the Cambridge team demonstrated it [3]. The
challenge today is to go beyond the static aspect of TEM by providing access to data followed by
temporal evolutions, thanks in particular to the development of *in situ* experimental devices. This
path is extremely promising because dislocations give rise to numerous interactions, between
them and with other defects (point defects, grain boundaries), that can only be understood at the

---

[*] Corresponding author.

TEM scale and in 3D. On scalar objects, the first 4D (i.e. time resolved) electron tomography was performed in 2010 [4], but this technique could not yet be applied to dislocations imaged with a diffraction contrast. An elegant approach to this question has been provided by combining the dynamic side of *in situ* straining experiments applied to configurations otherwise characterized in tomography [5]. More recently, morphological evolutions of dislocations by simultaneously combining *in situ* deformation and tomography has been captured [6]. However, the dislocation reconstruction quality did not allow advanced characterization.

Here, we report the development of 4D electron tomography of dislocations to study the first stages of formation of helical dislocations resulting from electron irradiation. To that purpose, we rely on a new method to perform electron tomography with few projected images [7], hence reducing drastically the acquisition time. In addition, we show that if the sampling is efficient enough and the system does not evolve in a too complex manner between two acquisitions, it is possible by interpolation to synthesize intermediate images and thus produce continuous 4D descriptions of the evolution of the system (Movies S1 and S2).

2. Materials and methods

2.1. *Deformation experiment*

The specimen investigated in this study has been deformed under high pressure in a multianvil apparatus (5000 t press) at the Bayerisches Geoinstitut, University of Bayreuth, Germany. The specimen was cut from a single crystal of MgO kindly provided by S. J. Mackwell. It was placed in a 14 M high-pressure assembly in between two hard alumina pistons to generate deviatoric stresses during compression [8]. The [100] axis of the crystal was along the axis of the assembly, i.e. along the principal compression axis. The assembly was compressed two hours at 1500 °C and a confining pressure of 10 GPa. At the end of the run, the temperature was quenched and pressure was released slowly to prevent fracturing.

2.2. *Thin foil preparation for TEM analyses*

A thin foil for TEM analyses was prepared by cutting a 250 μm thick slice from the specimen, at 45° from the principal compression direction, close to the orientation (101). This thick section was then mechanically polished down to ca. 30 μm thickness. The thin foil was first deposited on a 100 mesh Mo TEM support grid for ion thinning until electron transparency. For tomographic acquisition, the resulting foil has been transferred to a 100 mesh/100 mesh Cu folding grid chosen to ensure a good thermal conductivity during heating. Then, a thin amorphous carbon layer was spread on the thin foil to allow electron conduction.

2.3. *Dislocation electron tomography acquisition methods*

TEM investigations were conducted with a FEI® Tecnaï G^2-20 twin microscope operating at 200 kV with a LaB_6 filament. Tilt-series were acquired at room temperature and 650 °C with a Gatan® double-tilt heating sample-holder model 901. A perfect alignment of the diffraction vector used to generate the diffraction contrast, along the sample-holder principal axis, is required to perform dislocation electron tomography [9]. With this alignment, the diffraction contrast conditions are kept constant all over the tilt-series acquisitions. Tilt-series have been acquired every 5° with an average tilt angle ranging from −35° to 25° in weak-beam dark-field and bright-field conditions. The g: 11$\bar{1}$ diffraction vector has been chosen due to its high structure

factor. *In situ* electron irradiation conditions were performed at 650 °C with the largest condenser aperture (200 μm in diameter) and the largest spot size (180 nm in diameter). The electron beam was focused on the area of interest with a diameter of 3.4 μm, which produces a fluence of ca. 3.35×10^4 electron·nm^{-2}·s^{-1}. Four tilt-series have been acquired on the same zone. The acquisition of the first tilt-series has been performed at room temperature with an unfocused electron beam (i.e. under low irradiation conditions). The second tilt-series has been acquired at 650 °C following an electron beam exposure of 15 min (exposure dose of approximately 3.0×10^7 electron·nm^{-2}). The acquisitions of the third and fourth tilt series have been obtained at the same temperature following electron beam exposures of 45 and 105 min respectively (cumulated exposure doses of approximately 9.0×10^7 and 21.1×10^7 electron·nm^{-2} respectively).

2.4. *Dislocation electron tomography post-processing methods*

Dislocation electron tomography reconstructions with few projected images require a specific post-processing methodology. Accurate tilt series alignments (spatial errors lower than 3 nm) have been performed manually on several areas in order to keep the tilt axis close to the dislocations of interest. Then, our procedure exploits the particularities of dislocations with respect to tomography. Contrary to other tomography studies, the one applied to dislocations does not aim at reconstructing a physical object as a particle, but a linear elastic singularity that is imaged by a diffraction contrast. This contrast is an artifact that can present complex peculiarities (such as an oscillating contrast depending on the position in the slide) but which allows us to locate the projection of the line position. In order to free ourselves from these parasitic contrasts and to concentrate on the fundamental parameter of our study, the line position, we redraw each dislocation line for each projected image before the tomographic reconstruction. This allows us to obtain images with a discrete black and white contrast before the tomography reconstruction performed employing the weighted back-projection algorithm [10]. This algorithm is freely available on the TomoJ plugin [11]. Since the reconstruction algorithm extrapolates the dislocation positions in tilt-series missing-wedges, the resulting reconstructed dislocation thicknesses are thicker in these angular ranges. Consequently, raw reconstructed dislocations appear as ribbons (Figure 1) whose intensity distribution, however, allows the position of the line to be located precisely. The free UCSF Chimera software gives the possibility to select the highest gray value of the voxels where the image of the dislocation core is still discernible (see Figure 1C) and to redraw each dislocation into the raw reconstructed volumes [12,13]. This procedure restores dislocation cylindrical geometries (see Figure 1D). Nevertheless, it should be kept in mind that the dislocation segments oriented perpendicularly to the tilt axis (i.e. horizontally in Figure 1) generate the highest reconstructions inaccuracies (small black arrow on Figure 1C). Consequently, the horizontal dislocation segments are not considered in this study. In this paper, since the kinetics is not too fast and since we want to track subtle changes of the dislocation shapes, we have used 10 to 12 images to ensure the highest reliability of the reconstruction. This number can be reduced to optimize the acquisition process and make it faster to follow faster dynamics. We show in Figure 2 that reducing the number of images from 10 to 2 leads to a very small degradation of the reconstruction quality.

2.5. *Visualization*

In order to follow the dislocation character evolution during irradiation, a color has been affected to each dislocation segment which varies with the angle between the line and the Burgers vector. The color code has been chosen to range from blue for the pure screw character to red for the pure edge. To improve the 4D visualization movies, interpolations of reconstructed volumes between
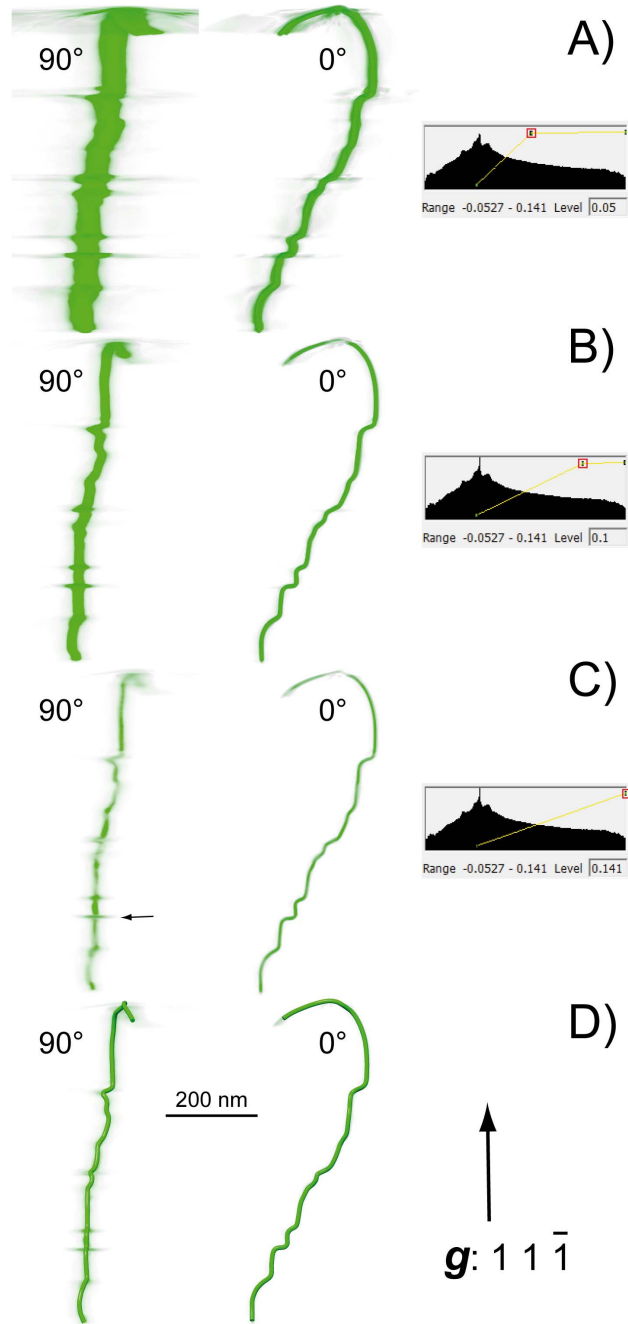
Figure 1. (Color online) Methodology used to trace dislocation lines with the Chimera software considering the uncertainty related to the missing wedge. (A) Raw reconstructed volume (from Figure 4) for two projected angles (90° and 0°) with a gray value of 0.05 (32-bit image) the ribbon resulting from the missing wedge is clearly visible at 90°. (B) With a gray value of 0.1, the extension of the ribbon is reduced. (C) With the highest accessible gray value (0.141), the position of the dislocation can be determined with accuracy, even at 90°. (D) Superimposing the traced dislocation on the raw reconstructed volume from Figure 4C (45 min irradiation). The diffraction vector is indicated by the vertical black arrow.

Figure 2. (Color online) Comparison between the reconstructed green volume obtained with 10 projected images (−35°, −25°, −20°, −15°, −5°, 0°, 5°, 10°, 15° and 25°) and the reconstructed purple volume obtained with 2 projected images (−35° and 25°). The diffraction vector is indicated by the black arrow.
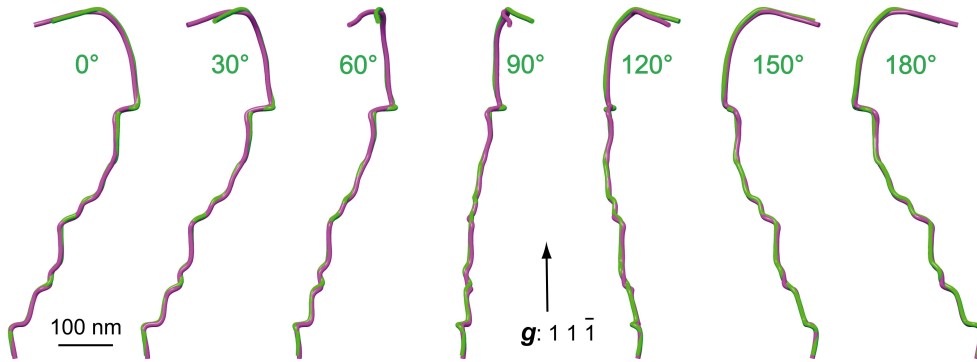
the four electron irradiation conditions are conducted using the DAIN-App (Depth-Aware video frame INterpolation) free software [14] based on artificial intelligence.

3. Results

3.1. *Electron tomography of dislocations with few images*

The challenge of electron tomography of dislocations (ETD) is to minimize the data acquisition time in order to allow tracking with the best temporal resolution. In this perspective, the development of ultra-fast cameras represents a major step forward [15]. Yet, ETD requires acquisition of a large number of images with a diffraction contrast adjusted with precision and this becomes the time limiting stage. In this study, we present a complementary improvement path which consists in decreasing the number of images and reducing the sampling angular range while preserving a high reliability of reconstruction. Details of the experimental protocols are given in the Materials and methods section. In a few words, the key points are to focus on the reconstruction of dislocations close to the tilt axis and to redraw the dislocations as white lines on a uniform black background before tomography reconstruction with the weighted back-projection algorithm [10].

3.2. *Experimental study of dislocation evolution*

In this work we apply this methodology to the study, *in situ*, of the evolution of dislocations in a sample irradiated with electrons. It is well known that dislocations play the role of sinks and sources of point defects. The formation of helical dislocations after irradiation has been observed for a long time [16] and discussed theoretically [17–19] and numerically [20–22]. However, although the advanced (equilibrium), helical, form of dislocation in the presence of supersaturation or undersaturation of point defects is well established [17], the mechanisms of nucleation are rather poorly documented from an observational point of view. Helical dislocations can indeed be formed by the reaction of a screw dislocation with prismatic loops [17, 20], or by the climb of mixed segments pinned at their ends [23, 24].

We used in this study a MgO sample deformed at 1500 °C and 10 GPa and containing a dislocation density of 2×10^{13} m^{-2}. We annealed this sample *in situ* at 650 °C in the microscope while focusing the electron beam on the areas of interest. The tomographies were recorded after 15 min, 45 min and 105 min of irradiation which corresponds to cumulative doses of 3.0×10^7, 9.0×10^7 and 21.1×10^7 electron·nm^{-2}. Figure 3 is a schematic representation of our experiments.
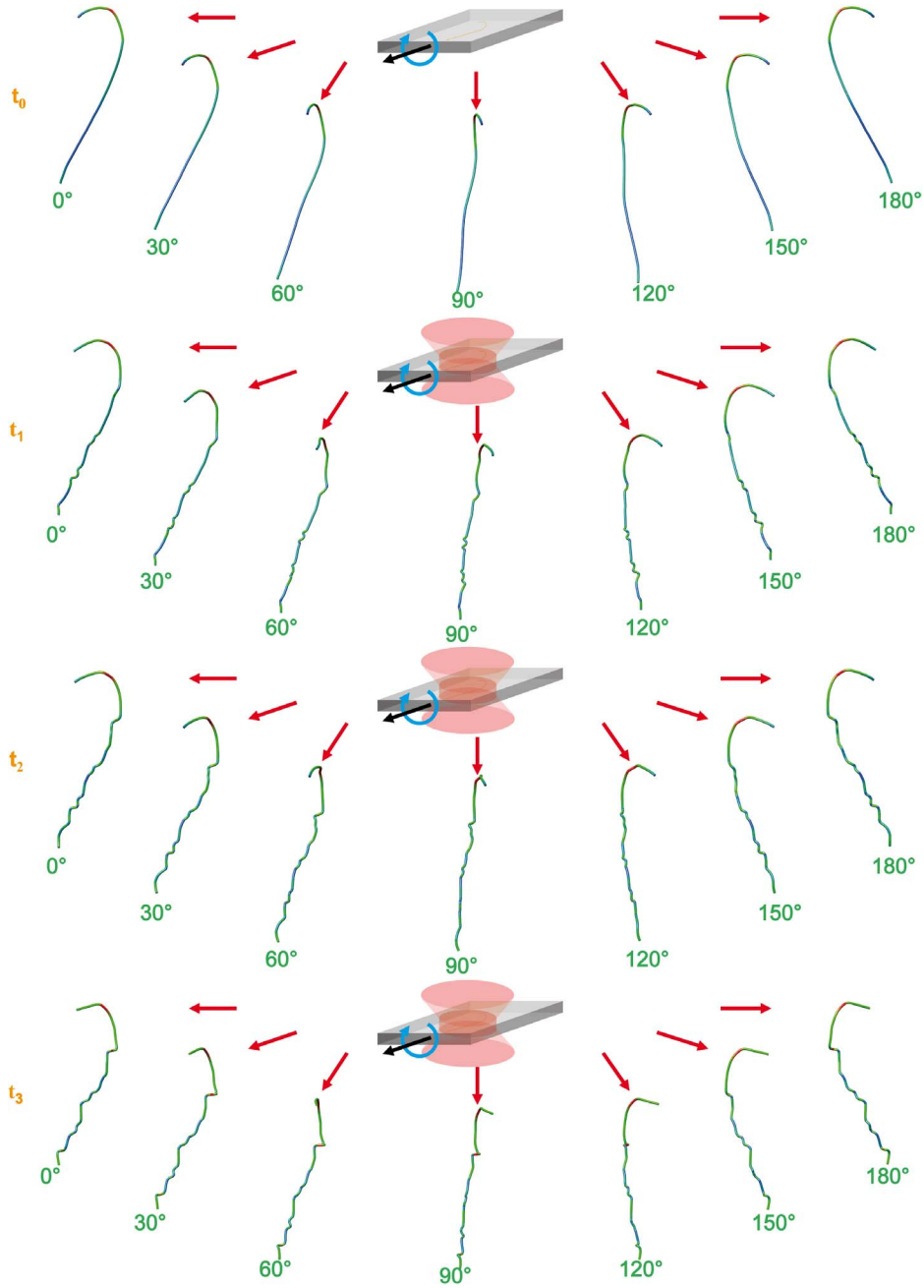
Figure 3. (Color online) Schematic representation of time-resolved 4D electron tomography of a dislocation undergoing annealing and electron irradiation. (A) t_0 represents initial conditions where the 3D structure of a given dislocation is presented under seven viewing angles ranging from 0 to 180°. (B) t_1 corresponds to 15 min of irradiation at 650 °C corresponding to an electron dose of 3.0×10^7 electron·nm^{-2}. (C) t_2 corresponds to 45 min of irradiation at 650 °C (electron dose 9.0×10^7 electron·nm^{-2}). (D) t_3 corresponds to 105 min of irradiation at 650 °C (electron dose 21.1×10^7 electron·nm^{-2}). Movie S1 displays a continuous evolution with time of this dislocation viewed in 3D.
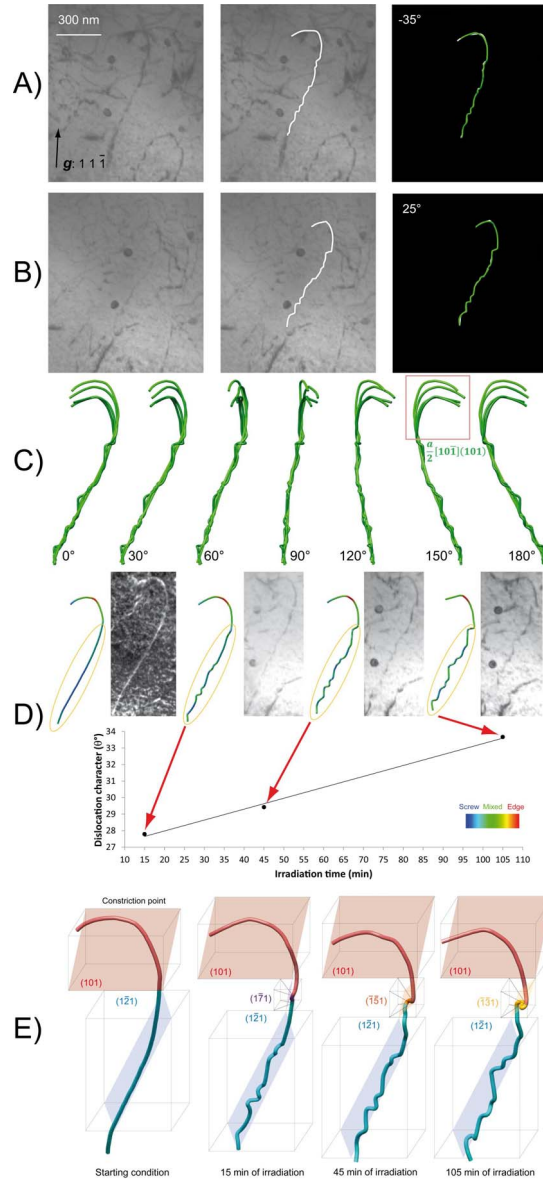
Figure 4. (Color online) Evolution of a $1/2[10\bar{1}]$ dislocation under electron irradiation. The dislocation is seen at $-35°$ in (A) and $25°$ in (B) (both at 45 min irradiation). Left is the raw image, in the middle is the tracing superimposed to it and right is the tomographic model superimposed to the tracing. (C) Superimposition of the four tomographic models at 0, 15, 45 and 105 min irradiation time at 650 °C. Evolution of the upper part in the red square is presented in greater details in Figure 6. (D) Shows the dislocation character with a color gradient (inset) for the dislocation viewed at 0°. The graph shows that the average dislocation character evolves linearly with irradiation time toward more edge components. (E) Indexing of the planes containing the dislocations segments. The upper part (in red) is contained in (101) while the lower part (in blue) is in $(1\bar{2}1)$ revealing cross-slip of the initial configuration. The evolution of the segment located in between is shown. The 3D evolution of the blue segment is described in more details in Figure 11A.

Figure 5. (Color online) Illustration of the main steps of tomographic reconstruction for the seven dislocations presented in Fig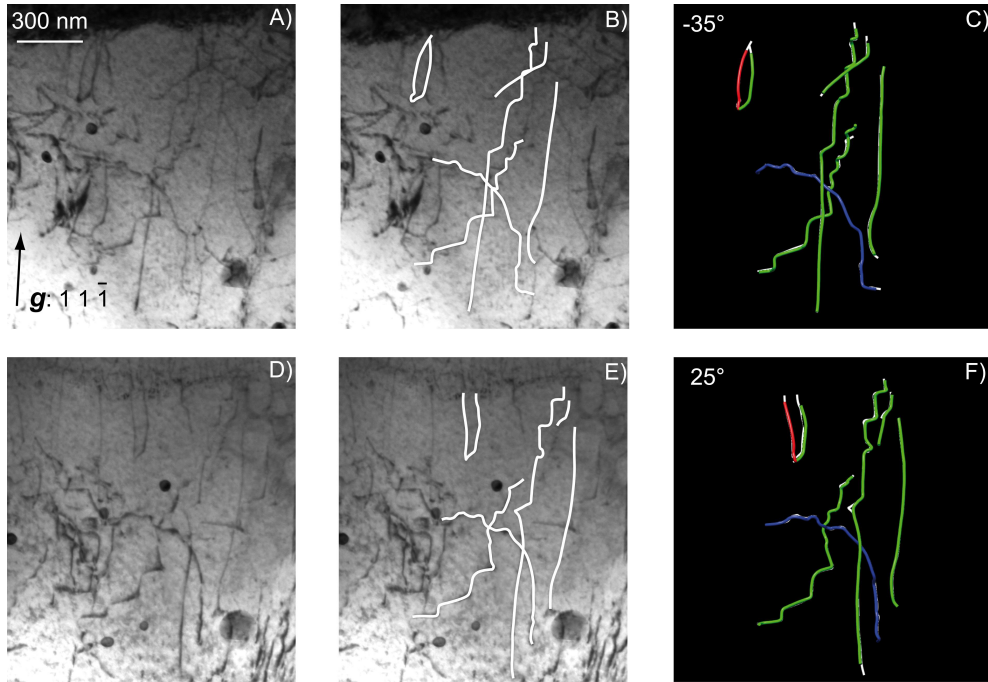ure 7 (Irradiation time 105 min). Left is the raw image, in the middle is the tracing superimposed to it and right is the tomographic model superimposed to the tracing. (A, B, C) Correspond to −35°. (D, E, F) Correspond to 25°.

Figure 4 illustrates our post-processing protocol on a dislocation that evolves significantly during irradiation at 650 °C. We see, for two different projection angles (−35° (Figure 4A) and 25° (Figure 4B)), the dislocation traced and the model resulting from the tomographic reconstruction (for more details see the Materials and methods section and see also Figure 5). This dislocation consists of a long segment, originally quite straight, and a second segment very curved. The Figure 4C shows the superposition of all the configurations of this dislocation during irradiation. The evolutions of shape and position are clearly visible. The temporal sampling is sufficient to capture well the evolution of the dislocation shape. It is therefore even possible to interpolate between these different observations and to make a film that shows continuously the evolution of the dislocation during the irradiation (see Movie S1). The tomographic reconstruction is a model that allows the complete analysis of the dislocation geometry and its evolution under irradiation. In particular, we have the knowledge at each point of the dislocation line orientation. We can therefore deduce, always at each point of the line, the character of the dislocation, i.e. the angle that the line makes with its Burgers vector. This is illustrated in Figure 4D where the character is represented by a color gradient. It can be seen that the long segment of the dislocation (circled in yellow in Figure 4D), originally close to the screw orientation, develops more and more edge characters during irradiation. The proportion of edge characters evolves linearly with irradiation time (Figure 4D). The curved segment (upper part), which is mostly made up of mixed segments with strong edge components, sees little change in its characters, but its position does change. Figure 4E shows the analysis of the geometry of this dislocation. It can be seen that the curved segment (shown in red in Figure 4E) is originally in the (101) plane and that it remains in it during
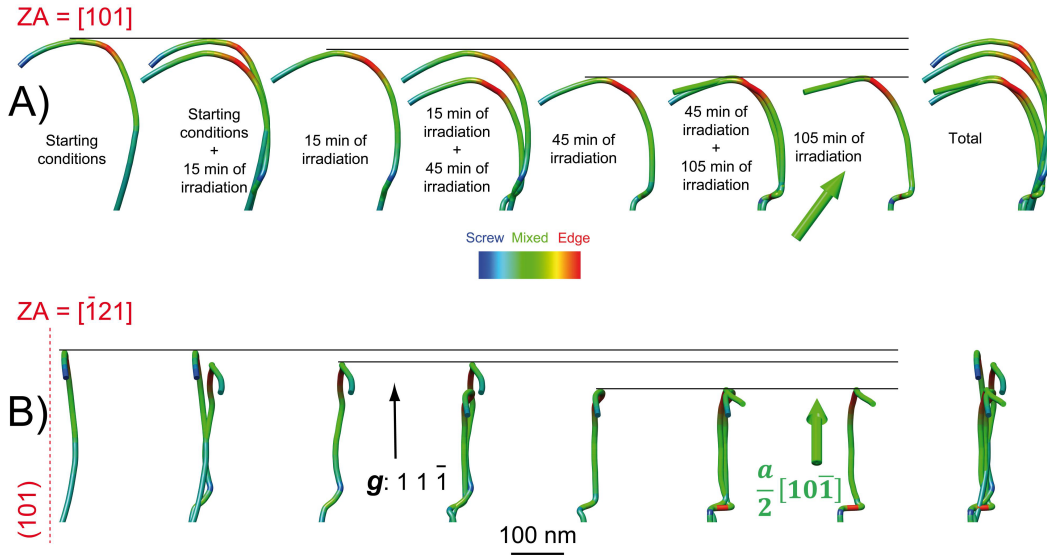
Figure 6. (Color online) Detailed study of the glide evolution of the upper part of the dislocation described in Figure 4 (in the red square of Figure 4(C)). (A) Evolution seen in the (101) glide plane. (B) The (101) glide plane is edge-on. The colors correspond to the character from blue (screw) to red (edge). The diffraction vector is indicated by the black arrow. The Burgers vector 1/2[10$\bar{1}$] is indicated by the thick green arrow.

its displacement (see also Figure 6). The (101) plane, being a natural glide plane for a dislocation of Burgers vector 1/2[10$\bar{1}$], the modification as recorded for this segment corresponds to pure glide resulting from the occurrence of internal stresses in the thin foil and facilitated by heating (650 °C). The long rectilinear segment (blue in Figure 4E) is in the (1$\bar{2}$1) plane. It is therefore also a glide configuration, and this dislocation thus indicates a cross-slip event. The (1$\bar{2}$1) plane has indeed already been reported as a cross-slip plane [25, 26], but not as one of the easiest slip plane. It can therefore be assumed that the lattice friction is higher there than in (101), which is why no glide is observed and edge segments develop. Another observation supports the hypothesis that the development of helixes by climb mainly affects segments with little mobility. This is the constriction point of the cross-slip between planes (101) and (1$\bar{2}$1). This segment, at the intersection of two glide planes is indeed geometrically immobile. We can see (Figure 4E) that it is the site of important changes in planes from (1$\bar{7}$1) to ($\bar{1}$5$\bar{1}$) and then ($\bar{1}$3$\bar{1}$). This evolution involves planes with increasing climb components (decreasing angle between the Burgers vector and the plane normal). Other gliding patterns were observed. They all involve dislocations belonging to easy MgO slip systems and in these cases, climb is only observed after the dislocation stopped gliding. This is the case of dislocation 1/2[10$\bar{1}$] (marked by α in Figure 7A). This dislocation is contained in the plane (101) and is engaged in a junction with dislocation 1/2[0$\bar{1}$1]. This reaction produces a dislocation 1/2[1$\bar{1}$0] which is not in contrast with the diffraction vector we have used (it is indicated as dashes in Figure 7A). This dislocation moves clearly although pinned by the junction (see also Figure 8). Another event related to a slip system of the same type (1/2[110](1$\bar{1}$0)) is indicated by γ in Figure 7A (see also Figure 9). Finally, we observe the same behavior for another segment gliding in (010) (β dislocation in Figure 7A), which corresponds to the second easy glide plane in MgO (see also Figure 10). In conclusion, the dislocations engaged in easy-gliding configurations of the structure glide, but do not climb as long as they have some capacity of
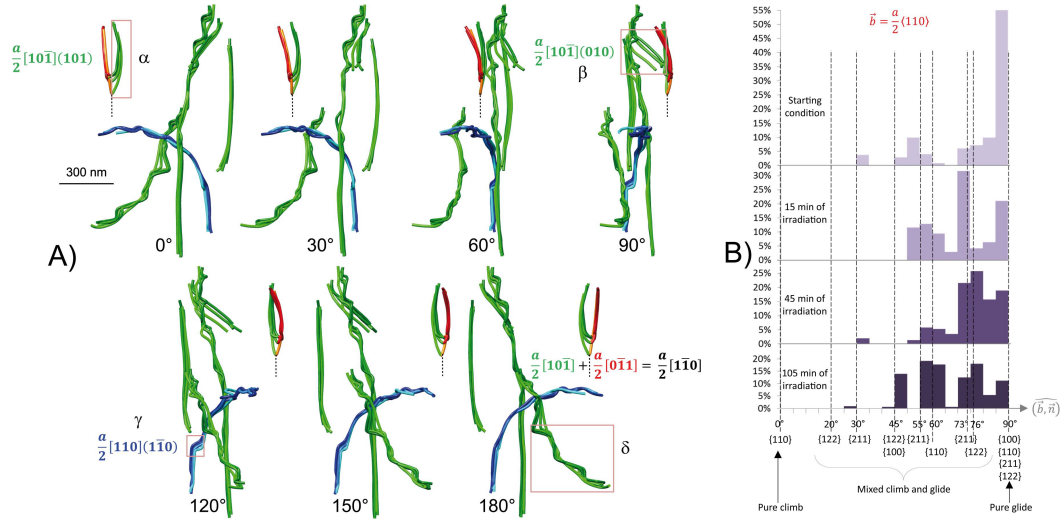
Figure 7. (Color online) (A) Evolution with irradiation of a zone containing seven dislocations (in contrast). Seven orientations are represented and the four tomographic models are superimposed. A 1/2[1$\bar{1}$0] dislocation resulting from a junction which is out of contrast is represented by a dashed line. Movie S2 shows how this microstructure evolves continuously with irradiation. Evolution of dislocations α, β and γ are presented in more details in Figures 8, 10 and 9 respectively. (B) Bar graph presenting the cumulated frequencies of planes containing dislocation segments as a function of the angle between the plane normal and the Burgers vectors. The gliding configurations are on the right (90°), the pure climb is on the left (0°). The intermediate configurations correspond to mixed climb.

gliding. These dynamic observations clearly show that the competition between glide and climb phenomena is linked to the effective mobility of the gliding dislocations.

3.3. *Observation of preferential mixed glide and climb planes*

We have tried to generalize this observation by accumulating the maximum number of characterizations on the modelled dislocations. We have thus characterized the largest possible number of planes containing segments of the dislocations studied considering the length of each dislocation segment. For each of these planes we calculate the angle between its normal and the Burgers vector of the dislocation concerned. 90° corresponds to pure glide and 0° to pure climb, all intermediate angles characterizing mixed climb. The results obtained are grouped in the bar graph of Figure 7B. Originally, the starting material mainly presents dislocations in glide configuration, even if, as a result of deformation at high temperature, some mixed glide planes are already indexed. As the irradiation progresses, a marked decrease in the occurrence of glide planes and the presence of mixed planes can be observed. One notes an evolution towards planes with more and more important climb components. However, this evolution does not seem to be continuous, and at each stage we note a high proportion of specific planes that are known to be glide planes of this structure (although for the Burgers vector concerned it is a mixed climb plane). The mixed climb is a phenomenon that is still little characterized [27]. Our observations suggest the presence of favorable planes. The cause is probably the core structure of the dislocations in mixed climb configuration (structure and geometry of jogs). Further observations and numerical modelling at the atomic scale will be necessary to verify this hypothesis.
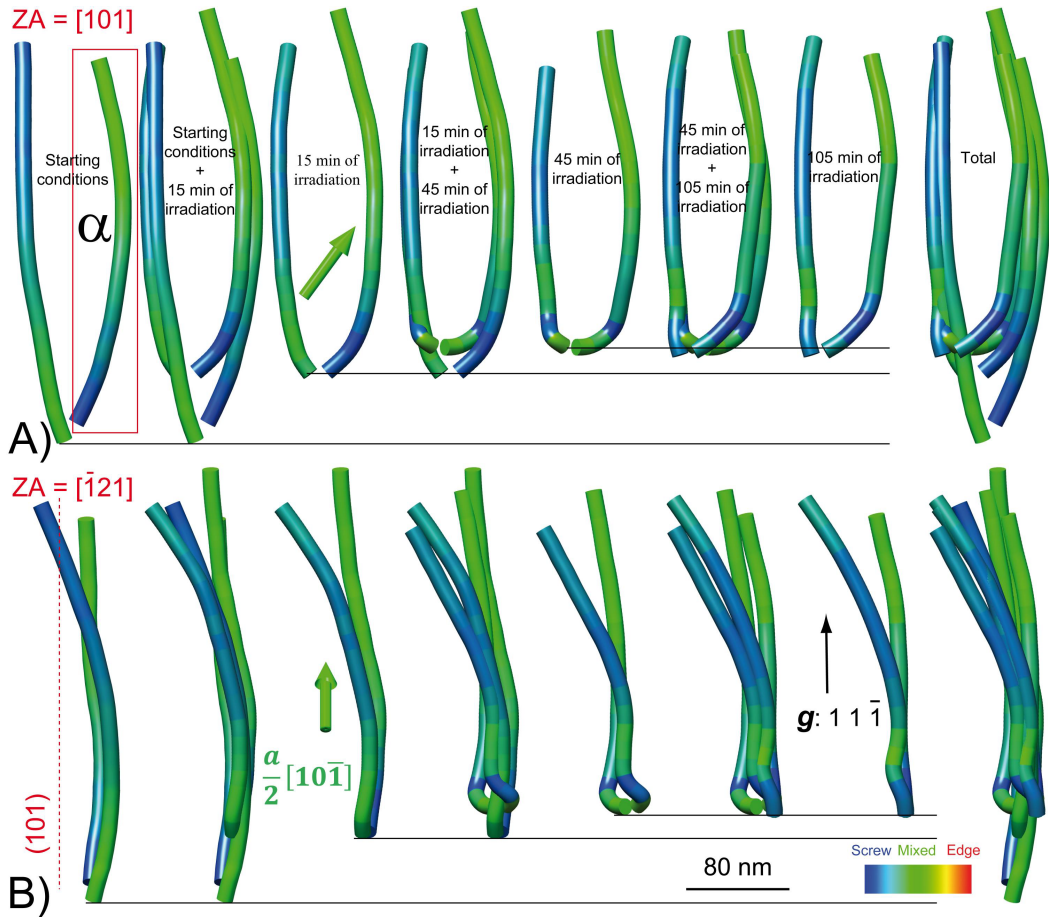
Figure 8. (Color online) Detailed study of the glide evolution of dislocation α with Burgers vector 1/2[1$\bar{1}$0] (green thick arrow) depicted in Figure 7. This dislocation is engaged in a junction with a dislocation which is shown here and resulting in a third dislocation which is out of contrast with the diffraction vector used (black arrow). (A) Evolution seen in the (101) glide plane. (B) The (101) glide plane is edge-on. The colors correspond to the character from blue (screw) to red (edge). The largest displacement is observed at the beginning of the experiment and then the dislocation stagnates.

4. Discussion

Helical dislocations reported in literature usually correspond to advanced stages, and are remarkably uniform in radius and wavelength [24, 28, 29]. Our 4D study allowed us to sample several stages in the early development of helical dislocations from dislocations with a strong screw character. Figure 4 shows two situations where such segments are isolated. With the tomographic model we visualize the dislocation along the dislocation segment whose shape becomes helical (Figure 11A, B). Under irradiation, the dislocation extends laterally and develops in a cylinder whose diameter increases. Internal stresses and point defect saturation under the electron beam initiate the development of edge components along the initial dislocation line. This is the beginning of the helix formation and, at this stage, the helix are not regular and not at equilibrium. We further validate this assumption by measuring the evolution of both the radius (r) of the cylinder
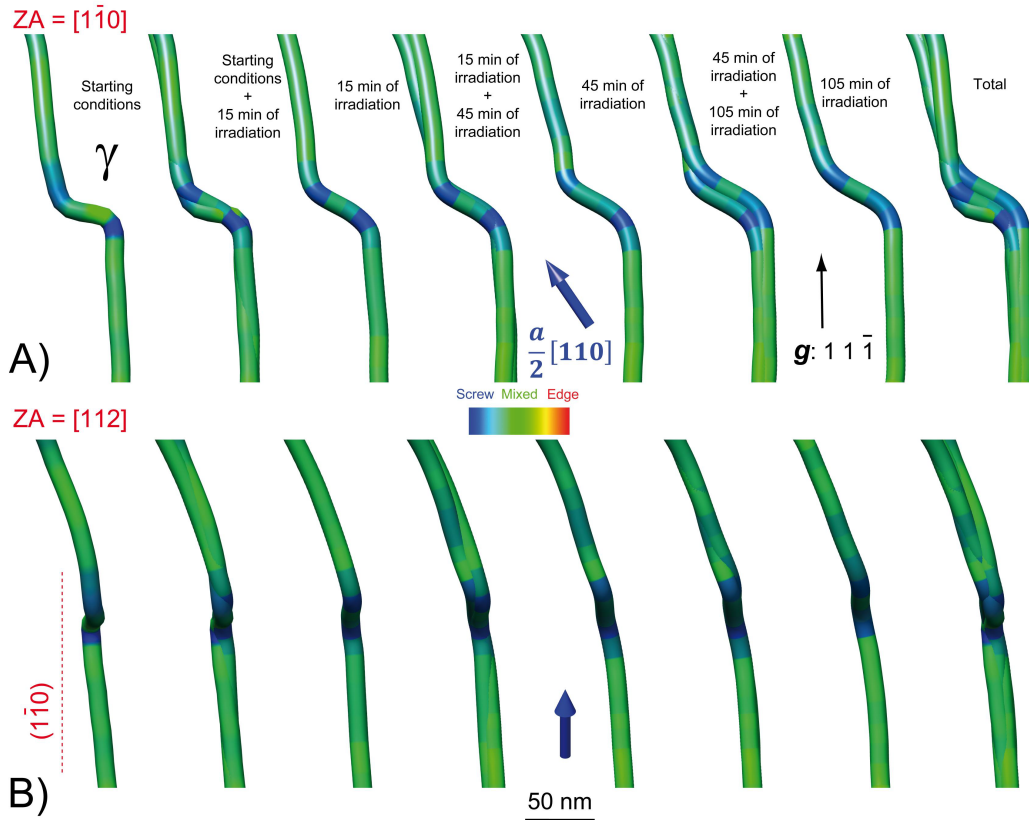
Figure 9. (Color online) Detailed study of the glide evolution of dislocation segment γ with Burgers vector 1/2[110] (green blue arrow) depicted in Figure 7. (A) Evolution seen in the $(1\bar{1}0)$ glide plane. (B) The $(1\bar{1}0)$ glide plane is edge-on. The colors correspond to the character from blue (screw) to red (edge). The diffraction vector is indicated by the black arrow.

the cylinder in which the helix is wound and the pitch of the helix (λ) as a function of the irradiation time (which scales with the dose received). It turns out that for five initially straight dislocations developing a helical shape, the ratios r^2/λ which intrinsically scales with the number of point defect absorbed per unit length [30], increase linearly with the irradiation time. As the flux of point defect is maintained, the helix growths toward a stable uniform cylindrical configuration. Throughout the observation time, the magnitude of the ratios λ/r is found in between 3 and 10, thus exceeding the theoretical value of 1.4 for well-developed equilibrated helixes [24, 28, 29]. However, such a configuration with $\lambda \gg r$ is typical of a growing helix for which the climb mechanism is dominant compared to glide processes [31]. This confirms that the development of the helical dislocation is indeed driven by the climb of some edge components.

The growth of helix results from a balance between the line tension of the dislocation and the elastic interaction between edge components along the helixes. Hence, at equilibrium, one would expect a point defect chemical potential for a supersaturation $c > c_0$ that maintains the helix shape expressed as $\xi/((2\pi r)^2 + \lambda^2)^{1/2} \sim kT \cdot \ln(c/c_0)$ (assuming the line tension ξ constant) [30]. This is consistent with our measurements showing that for the most developed helical dislocation the quantity $\xi/((2\pi r)^2 + \lambda^2)^{1/2}$ rapidly decreases and tends to saturate to a constant value corresponding to the equilibrium case of a uniform helix in equilibrium with a given point defect
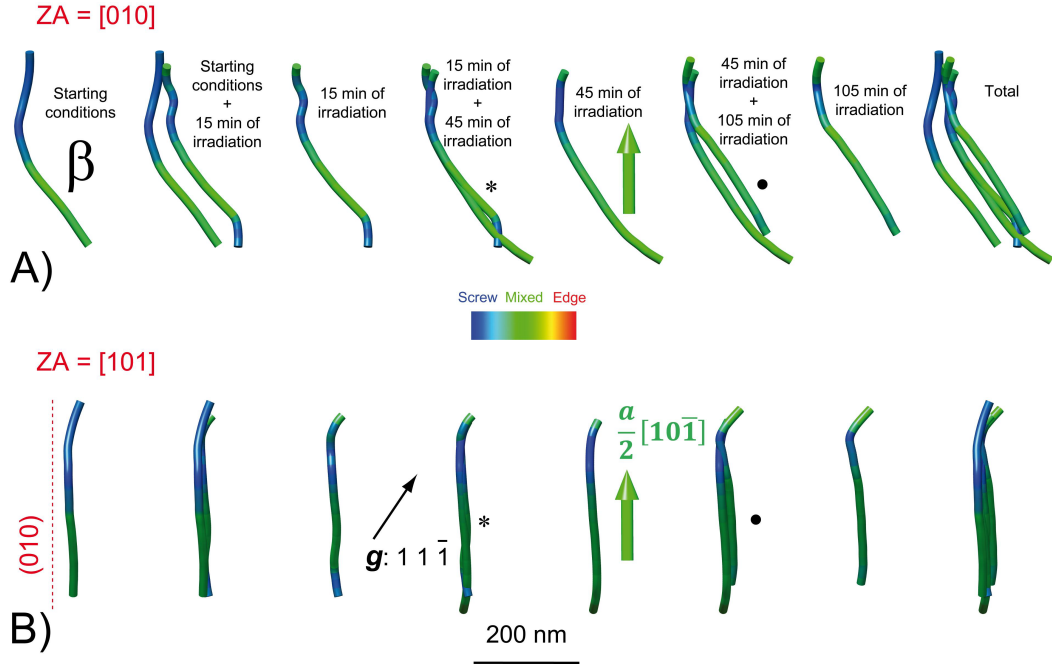
Figure 10. (Color online) Detailed study of the glide evolution of dislocation segment β with Burgers vector $1/2[10\bar{1}]$ (green thick arrow) depicted in Figure 7. (A) Evolution seen in the (010) glide plane. (B) The (010) glide plane is edge-on. The colors correspond to the character from blue (screw) to red (edge). The diffraction vector is indicated by the black arrow. The largest displacement is observed during the first stage of the experiment, then the dislocation stagnates during the additional 45 min of irradiation ($*$). Finally, during the last 105 min of irradiation, the dislocation moves slightly outside the glide plane by climb ($\bullet$).

chemical potential (Figure 11C, D). Here again, we note that the helix formation involves preferential orientations in particular planes. Figure 11B thus shows a preference for planes $(12\bar{1})$, $(11\bar{2})$ and (011). The occurrence of these peculiar orientations probably reflects lower dislocation core energies, although the validation of this hypothesis would require high accuracy atomistic calculations.

5. Conclusion

Plasticity is related to the displacement of dislocations in a crystal. Dislocations that are linear defects can adopt complex configurations in space and give rise to various interactions. 4D dislocation tomography, which combines three-dimensional imaging with time resolution, is an essential approach in this field. In the application demonstrated here, we document for the first time the initial mechanisms of helical loop formation under irradiation. We highlight the role of the mobility of dislocations on the initiation of climb. Indeed, this affects only the immobile segments, whether they are already not gliding, or whether they are in planes with high lattice friction or geometrically blocked (cross-slip node). We highlight the existence of preferential mixed climb planes not yet reported for MgO. The proof of feasibility brought by this paper calls for continuing developments towards ever faster acquisitions. The acquisition of discontinuous tilt-series will however always impose constraints on the kinetics available

Figure 11. (Color online) Helix formation. (A) Dislocation of Figure 4 seen along the direction of the long initially relatively straight segment (left) and perpendicularly (right). (B) Same for the segment marked by δ in Figure 7. (C) and (D) Represent (for (A) and (B) respectively) the evolution during irradiation of the geometrical parameter representative of the oversaturation of point defects (see text).

for study. For dislocation glide, for instance, the lattice friction that determines the speed of the dislocations will be a determining parameter. Observational access to dislocation dynamics opens up unprecedented coupling perspectives with numerical models of dislocation dynamics that will allow us to understand the origin of the properties of high-performance materials and to design better ones.

Acknowledgments

Supplementary data

Supporting information for this article is available on the journal's website under https://doi.org/10.5802/crphys.80 or from the author.

All raw data are available at https://doi.org/10.5281/zenodo.4497007.

References

[1] J. Miao, P. Ercius, S. J. L. Billinge, "Atomic electron tomography: 3D structures without crystals", *Science* **353** (2016), article no. aaf2157.

[2] D. Wrapp, N. Wang, K. S. Corbett, J. A. Goldsmith, C. L. Hsieh, O. Abiona, B. S. Graham, J. S. McLellan, "Cryo-EM structure of the 2019-nCoV spike in the prefusion conformation", *Science* **367** (2020), p. 1260-1263.

[3] J. S. Barnard, J. Sharp, J. R. Tong, P. A. Midgley, "High-resolution three-dimensional imaging of dislocations", *Science* **313** (2006), p. 319.

[4] O. H. Kwon, A. H. Zewail, "4D electron tomography", *Science* **328** (2010), p. 1668-1673.

[5] J. Kacher, I. M. Robertson, "Quasi-four-dimensional analysis of dislocation interactions with grain boundaries in 304 stainless steel", *Acta Mater.* **60** (2012), p. 6657-6672.

[6] S. Hata, H. Furukawa, T. Gondo, D. Hirakami, N. Horii, K. I. Ikeda, K. Kawamoto, K. Kimura *et al.*, "Electron tomography imaging methods with diffraction contrast for materials research", *Microscopy* **69** (2020), p. 141-155.

[7] A. Mussi, J. Gallet, O. Castelnau, P. Cordier, "Application of electron tomography of dislocations in beam-sensitive quartz to the determination of strain components", *Tectonophysics* **803** (2021), article no. 228754.

[8] P. Cordier, D. Rubie, "Plastic deformation of minerals under extreme pressure using a multi-anvil apparatus", *Mater. Sci. Eng. A* **309** (2001), p. 38-43.

[9] A. Mussi, P. Cordier, S. Demouchy, C. Vanmansart, "Characterization of the glide planes of the [001] screw dislocations in olivine using electron tomography", *Phys. Chem. Miner.* **41** (2014), p. 537-545.

[10] G. T. Herman, A. V. Lakshminarayanan, A. Naparstek, "Convolution reconstruction techniques for divergent beams", *Comput. Biol. Med.* **6** (1976), p. 259-271.

[11] C. Messaoudi, T. Boudier, C. O. Sanchez Sorzano, S. Marco, "TomoJ: tomography software for three-dimensional reconstruction in transmission electron microscopy", *BMC Bioinform.* **8** (2007), article no. 288.

[12] E. F. Pettersen, T. D. Goddard, C. C. Huang, G. S. Couch, D. M. Greenblatt, E. C. Meng, T. E. Ferrin, "UCSF Chimera—A visualization system for exploratory research and analysis", *J. Comput. Chem.* **25** (2004), p. 1605-1612.

[13] G. S. Liu, I. M. Robertson, "Three-dimensional visualization of dislocation-precipitate interactions in a Al–4Mg–0.3Sc alloy using weak-beam dark-field electron tomography", *J. Mater. Res.* **26** (2011), p. 514-522.

[14] W. Bao, W. S. Lai, C. Ma, X. Zhang, Z. Gao, M. H. Yang, "Depth-aware video frame interpolation", in *Proceedings of the IEEE Computer Society Conference on Computer Vision and Pattern Recognition*, 2019, p. 3698-3707.

[15] V. Migunov, H. Ryll, X. Zhuge, M. Simson, L. Strüder, K. J. Batenburg, L. Houben, R. E. Dunin-Borkowski, "Rapid low dose electron tomography using a direct electron detection camera", *Sci. Rep.* **5** (2015), article no. 14516.

[16] W. Bontinck, S. Amelinckx, "Observation of helicoidal dislocation lines in fluorite crystals", *Phil. Mag.* **2** (1957), p. 94-96.

[17] J. Weertman, "Helical dislocations", *Phys. Rev.* **107** (1957), p. 1259-1261.

[18] R. de Wit, "Self-energy of a helical dislocation", *Phys. Rev.* **116** (1959), p. 592-597.

[19] P. Guyot, "Frank loops and helical dislocations in quenched aluminium", *Phys. Stat. Sol. (a)* **5** (1971), p. 95-108.

[20] X. Y. Liu, S. B. Biner, "Molecular dynamics simulations of the interactions between screw dislocations and self-interstitial clusters in body-centered cubic Fe", *Scr. Mater.* **59** (2008), p. 51-54.

[21] L. B. Munday, J. C. Crone, J. Knap, "Prismatic and helical dislocation loop generation from defects", *Acta Mater.* **103** (2016), p. 217-228.

[22] F. Liu, Z.-L. Liu, P. Li, Z. Zhuang, "Numerical investigations of helical dislocations based on coupled glide-climb model", *Int. J. Plast.* **92** (2017), p. 2-18.

[23] S. Amelinckx, W. Bontinck, W. Dekeyser, F. Seitz, "On the formation and properties of helical dislocations", *Philos. Mag.* **2** (1957), p. 355-378.

[24] Z. Q. Feng, C. W. Lin, T. T. Li, X. Luo, G. L. Wu, X. X. Huang, "Electron tomography of dislocations in an Al–Cu–Mg alloy", *IOP Conf. Series: Mater. Sci. Eng.* **219** (2017), article no. 012018.

[25] U. Messerschmidt, F. Appel, "Dislocation motion and formation of dislocation structures during in situ deformation in a high voltage electron microscope", *Mat. Sci. Eng. A* **113** (1989), p. 409-414.

[26] C. Tromas, J. C. Girard, J. Woirgard, "Study by atomic force microscopy of elementary deformation mechanisms involved in low load indentations in MgO crystals", *Philos. Mag. A* **80** (2000), p. 2325-2335.

[27] J. Malaplate, D. Caillard, A. Couret, "Interpretation of the stress dependence of creep by a mixed climb mechanism in TiAl", *Philos. Mag.* **84** (2004), p. 3671-3687.

[28] P. Veyssière, J. Grilhé, "Experimental study of the influence of some parameters on the helical dislocation equilibrium in quenched alloys", *Acta Metall.* **19** (1971), p. 1047-1051.

[29] G. Wagner, V. Gottschalch, "Helical dislocations in Sn doped GaP epitaxial layers and their characterization by transmission electron microscopy", *Philos. Mag. A* **52** (1985), p. 395-406.

[30] J. P. Hirth, J. Lothe, *Theory of Dislocations*, John Wiley & Sons, New York, 1982.

[31] J. Grilhé, "Stabilité des dislocations hélicoïdales", *Acta Metall.* **12** (1964), p. 1081-1088.